Supplementary Information

Coherent Dynamics Unraveling Exciton-carrier Correlations in Orthorhombic Lead Halide Perovskite

Vandana Tiwari[1,2,3*], Fulu Zheng[4,5*], Zihui Liu[5,*], Pabitra K. Jayak[6], Michael Thorwart[7,8], R. J. Dwayne Miller[9], Hong-Guang Duan[5], & Ajay Jha[10]

[1] *Stanford PULSE Institute, SLAC National Accelerator Laboratory, Menlo Park, California 94025*

[2] *Department of Chemical Science, Linac Coherent Light Source, SLAC National Accelerator Laboratory, Menlo Park, California 94025*

[3] *Max Planck Institute for the Structure and Dynamics of Matter, Luruper Chaussee 149, 22761, Hamburg, Germany*

[4] *Bremen Center for Computational Materials Science, University of Bremen, Am Fallturm 1, 28359 Bremen, Germany*

[5] *Department of Physics and Institute of Modern Physics, Ningbo University, Ningbo 315211, China*

[6] *Tata Institute of Fundamental Research, 36/P, Gopanpally Village, Ranga Reddy District, Hyderabad 500107, India*

[7] *I. Institut für Theoretische Physik, Universität Hamburg, Notkestr. 9, 22607 Hamburg, Germany*

[8] *The Hamburg Center for Ultrafast Imaging, Luruper Chaussee 149, 22761 Hamburg, Germany*

[9] *The Departments of Chemistry and Physics, University of Toronto, 80 St. George Street, Toronto Canada M5S 3H6*

[10] *Rosalind Franklin Institute, Harwell, Oxfordshire OX11 0QX, United Kingdom*

(Dated: July 11, 2024)

In this Supplementary Information, we present global fitting approach, two-dimensional Fourier transform of residuals, Tukey-window Fourier transform, raw traces of the exciton, carrier and cross peak. Moreover, we show the calculation details of Raman modes and also the excited-state calculations of exciton and charge carrier band.

I. GLOBAL FITTING APPROACH

Multidimensional global fits of both experimental arrays of 2D spectra were performed in accordance with the available algorithm developed earlier [1]. A detailed description of the technique can be found in the Supplementary Information of Ref. [2]. In this method, a sequence of 2D spectra taken at different waiting times T are collected to form a three-dimensional array S(ω_τ, ω_t, T). This 3D array is then decomposed into a sum of two-dimensional decay-associated spectra $A_i(\omega_\tau, \omega_t)$ with individual exponential decays of correspondingly associated life times τ_i according to

$$\mathrm{S}(\omega_\tau, \omega_\mathrm{t}, \mathrm{T}) = \sum_\mathrm{i} \mathrm{A_i}(\omega_\tau, \omega_\mathrm{t}) \exp(-\mathrm{T}/\tau_\mathrm{i}). \tag{S1}$$

We apply the global fitting to the 2D electronic spectra of perovskite.

II. TWO-DIMENSIONAL FOURIER TRANSFORM OF RESIDUALS

To avoid a pulse overlap effect, we perform the fit at the starting time of 20 fs. The measured window extends up to 2 ps with a time step of 15 fs. To achieve a good fit, at minimal two exponential functions are used to fit the kinetics in the 3D data. 3D residuals are obtained after removing the kinetics obtained from the global fitting approach. We perform the Fourier transform of 3D residuals along the waiting time T. The resulting 2D patterns for particular

frequencies are shown in Fig. S1. The power spectra of the modes at 32, 48, 112 and 177 cm^{-1} are shown in (d), (e), (f) and (g), respectively.

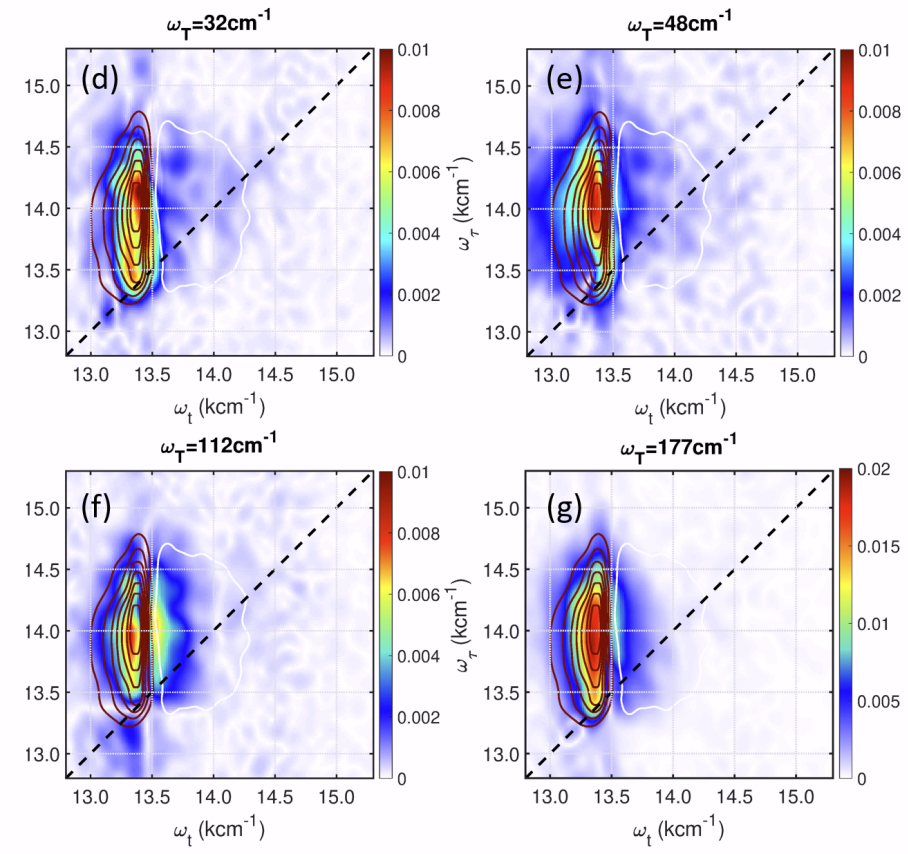

FIG. S1. Two-dimensional vibrational maps are shown in (d), (e), (f) and (g) with the resolved frequencies 32, 48, 112 and 177 cm^{-1}.

III. WAVELET ANALYSIS

In this section, we summarize the basic principles of the wavelet transform, the details of which have been described in Refs. [3, 4]. It starts from the definition of a zero-mean and short-time oscillating function ψ, called a "mother" wavelet, which is used to decompose a one- or multi-dimensional real-valued signal into different frequency bands. This mother wavelet function is translated in time by t and stretched by the scaling factor ω^{-1}, giving the wavelet "atom" function

$$\psi_{t,\omega}(t') = \sqrt{\omega}\psi\left([t'-t]\omega\right) . \tag{S2}$$

It provides the effective basis for the transformation. The two most common transforms are the discrete wavelet transform and the continuous wavelet transform CWT [5]. The discrete one decomposes the signal into several frequency bands and is frequently used for data and image compression. The continuous one, which is used in this paper, is based on an expansion of a temporal signal $f(t)$ via the inner product of the function with a wavelet atom,

$$CWT_f(t,\omega) = \int_{-\infty}^{+\infty} dt' f(t')\sqrt{\omega}\psi^*\left([t'-t]\omega\right) . \tag{S3}$$

The parameter t indicates where the wavelet atom is centered, while the scale parameter ω^{-1} controls the relative width of the wavelet atom compared to the mother wavelet function. This nonlinear integral transform provides a high time resolution of high-frequency components, while for the slowly varying components of the signal, the frequency resolution is high. It projects the signal onto basis functions with a varying "center" frequency and a varying range fixed by the scaling factor.

IV. TUKEY-WINDOW FOURIER TRANSFORM

Here, we provide the details related to the Fourier transform with the Tukey window. To isolate the high-frequency jitters, Fourier filtering in the frequency domain is employed. By this, we isolate each of these regions of interest with a Tukey window, which has the form

$$\omega(n) = \begin{cases} 1, & 0 \leq |n| \leq \alpha\frac{N}{2}\,, \\ \frac{1}{2}\Big(1+\cos\big[\frac{\pi(n-\alpha\frac{N}{2})}{(1-\alpha)\frac{N}{2}}\big]\Big), & \alpha\frac{N}{2} \leq |n| \leq \frac{N}{2}\,. \end{cases} \tag{S4}$$

Due to the flat top, it conserves the amplitudes of the Fourier components of interest over a larger frequency range than a cosine or a Gaussian window, while it still limits the artifacts arising from a pure bandpass filter. In this work, we use the Tukey window with $\alpha = 1/5$ and a Fourier bandpass filter with $\leq$700 cm^{-1}.

V. RAW TRACES OF THE CP, EXCITON AND CARRIER PEAKS

In this section, we show the raw traces of cross peak (CE), exciton (E) and carrier (C) in Fig. S2. The raw data have been plotted as the colored solid lines. The refinement has been performed with Tukey-window Fourier transform and the resulted data has been shown as cyan solid lines.

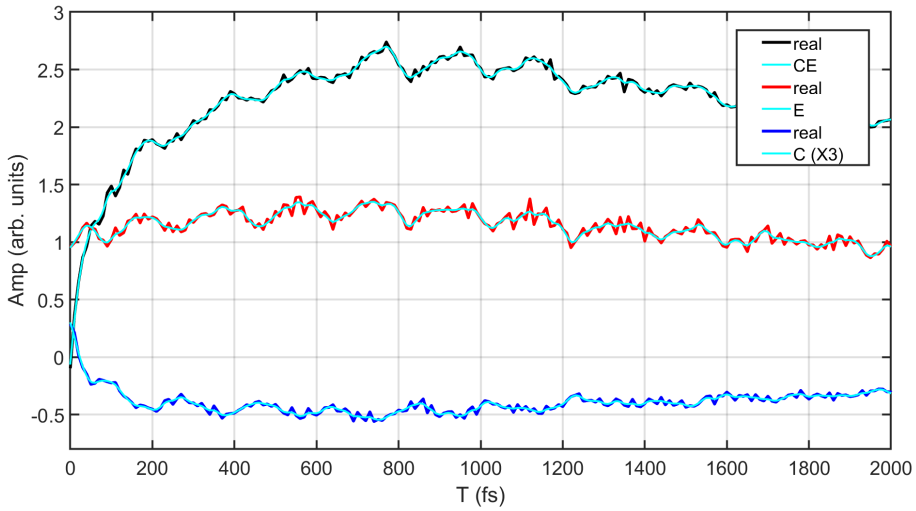

FIG. S2. Time-resolved traces of raw data, which have been plotted as colored lines. The processed data are shown as cyan solid lines.

VI. VIBRATIONAL COHERENCES IN 2D ELECTRONIC SPECTROSCOPY

In this section, we examine the vibrational coherences of the GSB and ESA peaks in the 2D electronic spectra. For this, we first construct a model of a three-level system, in which the electronic ground state, the first and second excited states are denoted by $|g\rangle$, $|e_1\rangle$ and $|e_2\rangle$, respectively. We assign the optical transitions between $|g\rangle$ and $|e_1\rangle$ and between $|e_1\rangle$ and $|e_2\rangle$ to mimic the response signals of the GSB (stimulated emission) and the ESA. Moreover, to study the coherent vibrational dynamics, the electronic ground and excited states are vibronically coupled to a vibrational mode. Here, we select an identified mode with a frequency of 180 cm^{-1}. By this, the system Hamiltonian is given as

$$H_S = |g\rangle\,\epsilon_g\,\langle g| + |e_1\rangle\,\epsilon_1\,\langle e_1| + |e_2\rangle\,\epsilon_2\,\langle e_2|\,, \tag{S5}$$

where ϵ_g, ϵ_1 and ϵ_2 are the site energies of the electronic ground, the first and second excited states, respectively. Moreover, a thermal reservoir of harmonic oscillators has been used to model the dissipative interactions with the

environment. Thus, we have

$$H_{B_1} = \sum_j \hbar\omega_j(\alpha_j^\dagger\alpha_j + 1/2),$$
$$H_{B_2} = \sum_j \hbar\omega_j(\beta_j^\dagger\beta_j + 1/2), \tag{S6}$$

where α_j ($\alpha_j^\dagger$) and β_j ($\beta_j^\dagger$) are the annihilation (creation) operators for the j-th bath mode with frequency of ω_j. For simplicity, we assume linear system-bath interactions, i.e.,

$$H_{SB_1} = |e_1\rangle\langle e_1| \sum_j c_j(\alpha_j^\dagger + \alpha_j),$$
$$H_{SB_2} = |e_2\rangle\langle e_2| \sum_j d_j(\beta_j^\dagger + \beta_j), \tag{S7}$$

where, c_j and d_j are the coupling strengths of j-th mode to the electronic state. In addition, we assume the frequency distribution of the baths to follow an Ohmic form with a Debye cutoff. Thus, the spectral density of each bath can be written as

$$J(\omega) = \frac{\hbar\eta_1}{\pi}\frac{\gamma_1^2\omega}{\gamma_1^2+\omega^2} + \frac{\hbar\eta_2}{\pi}\frac{4\gamma_2^2\omega_0^2\omega}{(\omega^2-\omega_0^2)+4\gamma_2^2\omega^2}, \tag{S8}$$

where $\eta_{1/2}$ and $\gamma_{1/2}$ are the coupling and damping constants, respectively. ω_0 is the frequency of a particular mode coupled to electronic states. To calculate this model, we assume $\epsilon_g = 0$, $\epsilon_1 = 800$ cm^{-1} and $\epsilon_2 = 2100$ cm^{-1}. In addition, we assume $\eta_1 = 1$, $\gamma_1 = 100$ cm^{-1}, $\eta_2 = 2$, $\gamma_2 = 20$ cm^{-1} and $\omega_0 = 500$ cm^{-1}. The transition diple is chosen as $\mu = |g\rangle\mu_{ge_1}\langle e_1| + |e_1\rangle\mu_{e_1e_2}\langle e_2|$. By this, we calculate the population dynamics and the 2D electronic spectra of this model using the hierarchy equation of motion [6, 7]. The details of this method and the way to calculate 2D electronic spectra have been described in Ref. [8]. We show the calculated 2D spectra in Fig. S3 for selected waiting times. In Fig. S3, we show that we are able to separate the ESA peak from the GSB peak completely by carefully selecting the site energies of ϵ_1 and ϵ_2. To examine the coherent dynamics, we extract the time-evolved amplitude of the GSB and ESA peaks, which are marked by "A" and "B" in Fig. S3 at T = 200 fs. We plot the traces of the GSB and ESA peaks as red and blue solid lines in Fig. S4. Moreover, we perform the global fitting on time series of the calculated 2D spectra. The fitted traces are shown in Fig. S4 as black dashed lines. The obtained residuals are shown in Fig. S5. In Fig. S5, we clearly observe the opposite phases of the oscillations in the residuals of the GSB and ESA peaks, respectively. By this, we demonstrate the anti-corrlated phases of the vibrational coherences of the optical signals from the GSB and ESA peaks in the 2D electronic spectra. Although it is based on a simple three-level model, we believe that this uncovered phase relation can be extended to the optical transitions between the valence and conduction bands in solid state dynamics.

VII. RAMAN SPECTRUM

Simulated Raman spectrum is shown in Fig. S6. The two modes with frequencies around 100 cm^{-1} are also presented in the bottom row of Fig. S6.

VIII. NON-ADIABATIC MOLECULAR DYNAMICS (NAMD) SIMULATIONS

The "hot" carrier cooling and electron-hole recombination dynamics in the perovskite at 15 K are investigated via non-adiabatic molecular dynamics simulations within the neglect of back reaction approximation (NBRA) [9]. We first obtained a 1000-steps (step size 0.5 fs) NVT molecular dynamics (MD) trajectory of the system at the desired temperature, i.e., 15 K. The nuclear coordinates and velocities from the last snapshot of the NVT trajectory are then used to initiate a NVE simulation for 20000 steps. As shown in Fig. S7, the temperature in the last 10000 NVE steps is oscillating around 15 K and the total energy almost remains constant, indicating that the system reaches a quasi-equilibrium state in this stage. Then 10000 nuclear conformations are extracted from this 5-ps production trajectory, and are used for electronic structure calculations.

The excited states of the system are obtained using the time-dependent density functional perturbation theory (TDDFPT) as implemented in the CP2K package. The energy and oscillator strength of the states from all configurations are then adopted to simulate the absorption spectrum of the system as presented in Fig. S8. The lowest four

states (S_1, S_2, S_3, and S_4) dominate the absorption spectrum with considerable oscillator strength. The S_1, S_2 and S_3 are mainly associated to the transitions from the valence band maximum (VBM) to the conduction band minimum (CBM), CBM+1, and CBM+2, respectively. S_4 has a quite close energy as S_3, and is dominated by the VBM-1 $\rightarrow$ CBM+1. The real-space distribution of the wave functions for aforementioned orbitals are shown in Fig. S9.

In addition to the time-dependent excited state energies, another key ingredient for NAMD simulations is the non-adiabatic coupling (NAC) between the adiabatic states. The NACs are evaluated by the Libra code [10] with the wave functions from TDDFPT calculations. The time-averaged absolute values of NAC is presented in the main text and the distribution of the absolute NAC values is given in Fig. S10.

With the time-dependent excited state energies and NACs between the states, the time-dependent Hamiltonian is constructed with the Libra code. The NAMD simulations are performed in turn in the framework of trajectory-based surface hopping approach [11] with different decoherence correction methods applied. Beyond Tully's fewest switches surface hopping (FSSH) scheme, we consider the decoherence effects via different methods, i.e., the modified simple decay of mixing scheme (mSDM) [13, 14], and the decoherence-induced surface hopping (DISH) method [12]. In order to take the effects of random nuclear configurations into account, we choose 200 snapshots from the Hamiltonian at the first 1000 time points as the starting frames. From each of these 200 frames, we launch 5000 surface hopping trajectories with an electronic initial condition.

For electron-hole recombination, initially the electronic population is localized on S_1. The averaged population on S_1 with different decoherence correction methods is illustrated in Fig. S11.

For "hot" electron cooling, a laser centered at the second lowest band ($E_{\rm ex}$=1.932 eV) with a full width at half maximum (FWHM) of 0.2 eV is adopted to mimic the excitation configuration. Such laser will simultaneously excite S_2, S_3 and S_4 with corresponding probabilities as the second lowest band is mainly contributed from these states (see Fig. S8). The unnormalized initial population of state i is determined by multiplying the oscillator strength f_i with a Gaussian-shaped Franck-Condon window (centered at $E_{\rm ex}$ with FWHM) as

$$P_i' = f_i \times \frac{1}{\sqrt{2\pi\sigma}} \exp\Big[-\frac{(E_i - E_{\rm ex})^2}{2\sigma^2}\Big], \tag{S9}$$

with FWHM $= 2\sqrt{2\ln 2}\sigma$ and E_i is the excitation energy of state i. The normalized initial excitation probability of state i is then obtained via $P_i = P_i'/\sum_i P_i'$. With the energies and oscillator strengths of S_2, S_3 and S_4 (as presented in Fig. S8), the initial populations of these states in "hot" electron cooling simulations are 0.4745, 0.2816, and 0.2439, respectively. We first perform NAMD simulations with initial population fully localized on individual states, and the population dynamics from three initial states is shown in the first three rows of Fig. S12. As S_3 and S_4 are quite similar in both energy and oscillator strength, the total population on these two states are presented in the plots. Then the initial excitation probabilities of S_2, S_3 and S_4 are adopted to weight the populations obtained from the above step, producing the final population dynamics from laser-generated initial conditions. As S_2, S_3 and S_4 dominate the second absorption band, the population dynamics of this band is obtained by summing the populations on these states, as dedicated by the solid red line in the lowest row of Fig. S12.

To estimate the time scales of the relaxation and recombination dynamics, as well as the effects of decoherence on these time scales, we fit the averaged population dynamics of the second band (total population on S_2, S_3, and S_4, for "hot" electron cooling) and S_1 (for recombination) using a sum of an exponential and a Gaussian function

$$p_f(t) = a \cdot {\rm e}^{(-t/\tau_1)} + (1-a) \cdot {\rm e}^{[-(t/\tau_2)^2]}, \tag{S10}$$

where a, τ_1, and τ_2 are fitting parameters. The parameter a, within range [0, 1], controls the ratio of the exponential component in the fitting function. The time scale of the dynamics is then obtained as $\tau = a \cdot \tau_1 + (1-a) \cdot \tau_2$. The time scales from fitting are presented in the plots with the fitting curve illustrated by the red-dashed lines.

[1] Prokhorenko, V. I. *European Photochemistry Association Newletter* June 2012, p21.
[2] Milota, F.; Prokhorenko, V. I.; Mancal, T.; Berlepsch, H. von; Bixner, O.; Kauffmann, H. F.; Hauer, J. J. Phys. Chem. A **117**, 6007 (2013).
[3] A. Cohen, and J. Kovačevič, Proc. IEEE 84, 514 (1996).
[4] J. D. Harrop, S. N. Taraskin, and S. R. Elliot, Phys. Rev. E **66**, 026703 (2002).
[5] J. van der berg, *Wavelets in Physics* (Cambridge University Press, 2004).
[6] Ishizaki, A. & Tanimura, Y. Quantum dynamics of system strongly coupled to low-temperature colored noise bath: Reduced hierarchy equations approach. J. Phys. Soc. Jap. **74**, 3131 (2005).
[7] Tanaka, M. & Tanimura, Y. Quantum dissipative dynamics of electron transfer reaction system: Nonperturbative hierarchy equations approach. J. Phys. Soc. Jap. **78**, 073802 (2009).

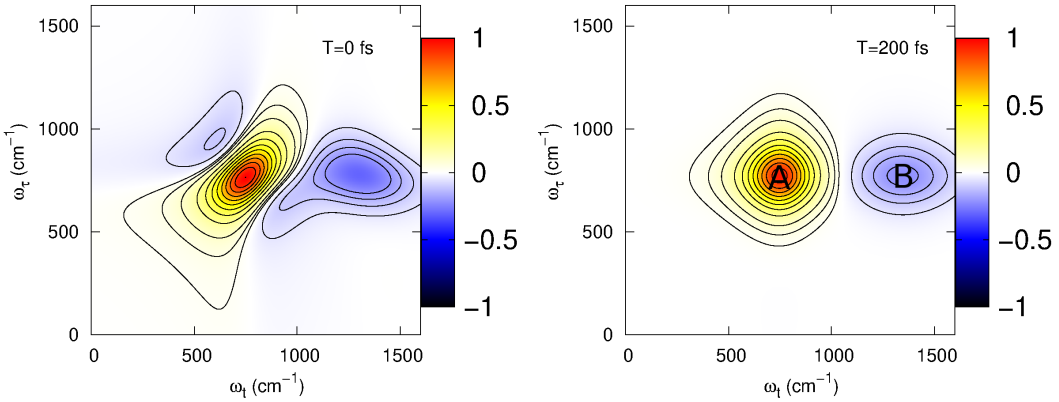

FIG. S3. Calculated 2D electronic spectra at T=0 (left) and 200 fs (right). The GSB and ESA peaks are marked by the positive and negative magnitudes in the 2D spectra.

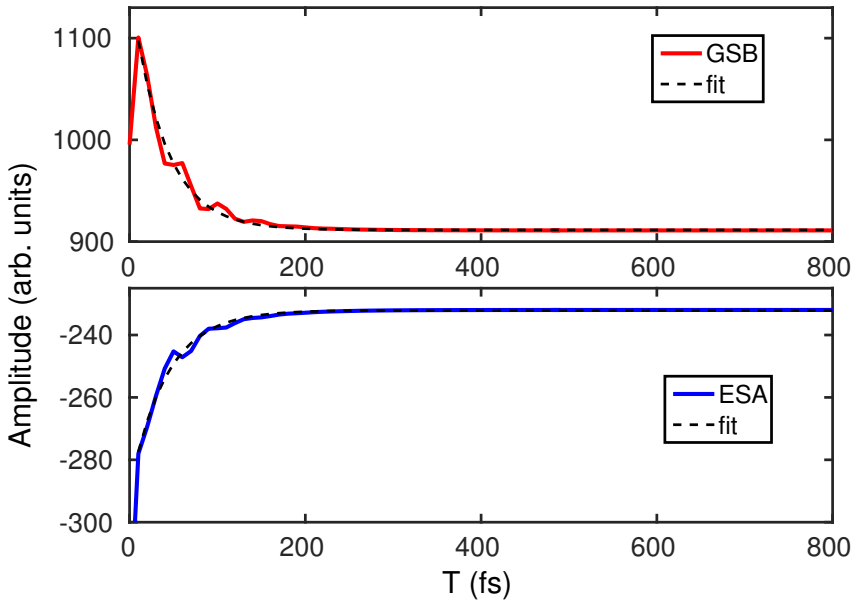

FIG. S4. The traces of the GSB (red solid line) and the ESA (blue solid line) from "A" and "B" in Fig. S3 at T=200 fs.

[8] Duan, H. G. & Thorwart, M. Quantum Mechanical Wave Packet Dynamics at a Conical Intersection with Strong Vibrational Dissipation. J. Phys. Chem. Lett. **7**, 382 (2016).

[9] C. F. Craig, W. R. Duncan, and O. V. Prezhdo, Trajectory Surface Hopping in the Time-Dependent Kohn-Sham Approach for Electron-Nuclear Dynamics. Phys. Rev. Lett. **95**, 163001 (2005).

[10] A. V. Akimov, Libra: An open-Source "methodology discovery" library for quantum and classical dynamics simulations. J. Comput. Chem. **37**, 1626 (2016).

[11] J. C. Tully, Molecular dynamics with electronic transitions. J. Chem. Phys. **93**, 1061 (1990).

[12] H. M. Jaeger, S. Fischer, and O. V. Prezhdo, Decoherence-induced surface hopping. J. Chem. Phys. **137**, 22A545 (2012).

[13] G. Granucci and M. Persico, Critical appraisal of the fewest switches algorithm for surface hopping. J. Chem. Phys. **126**, 134114 (2007).

[14] B. Smith, A. V. Akimov, A comparative analysis of surface hopping acceptance and decoherence algorithms within the neglect of back-reaction approximation. J. Chem. Phys. **151**, 124107 (2019).

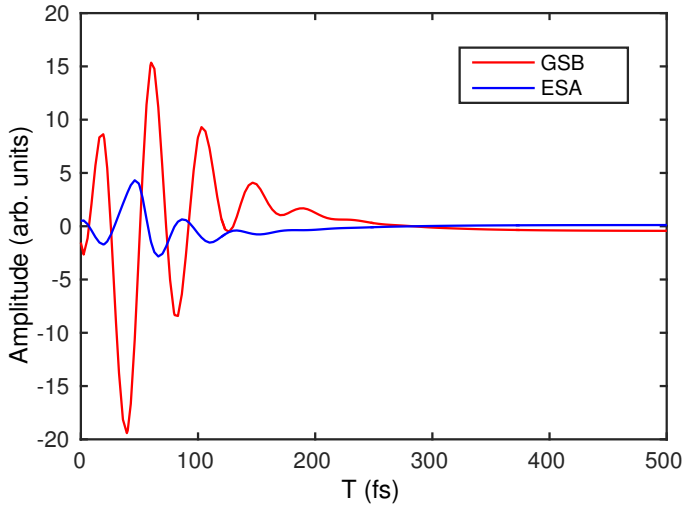

FIG. S5. Residuals of the GSB (red solid line) and the ESA (blue solid line) after removing the kinetics using a global fitting approach. They show opposite phases of oscillations of the GSB and ESA peaks.

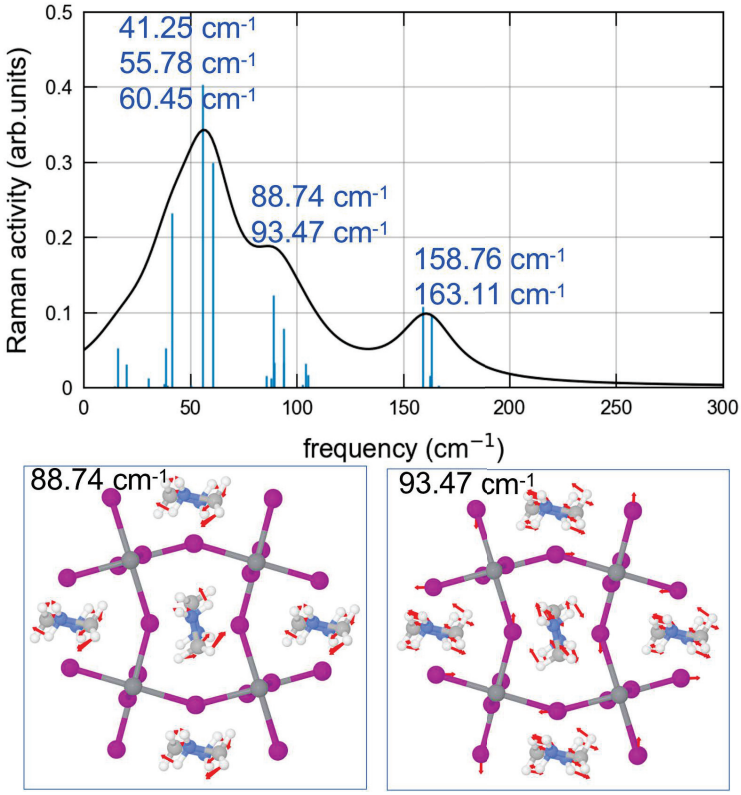

FIG. S6. Raman spectrum of the optimized structure and vector plots of modes at 88.74 cm^{-1} and 93.47 cm^{-1}.

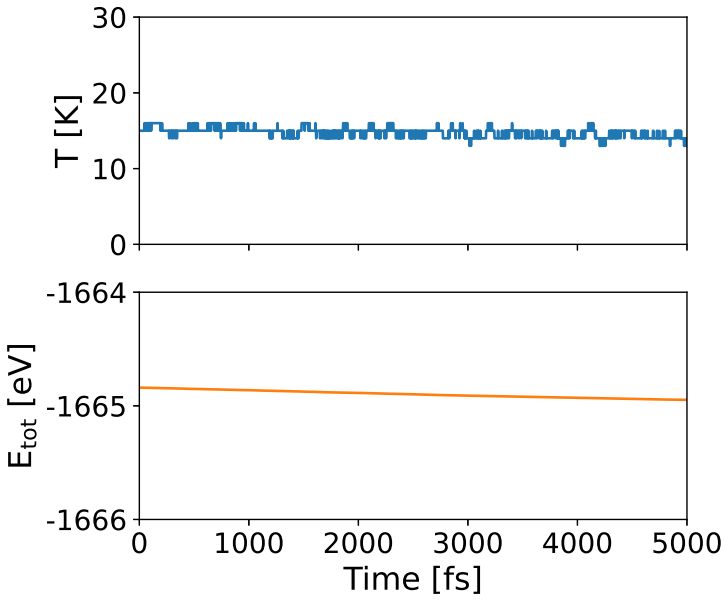

FIG. S7. Temperature (a) and total energy (b) of in the last 10000 steps of NVE MD simulation.

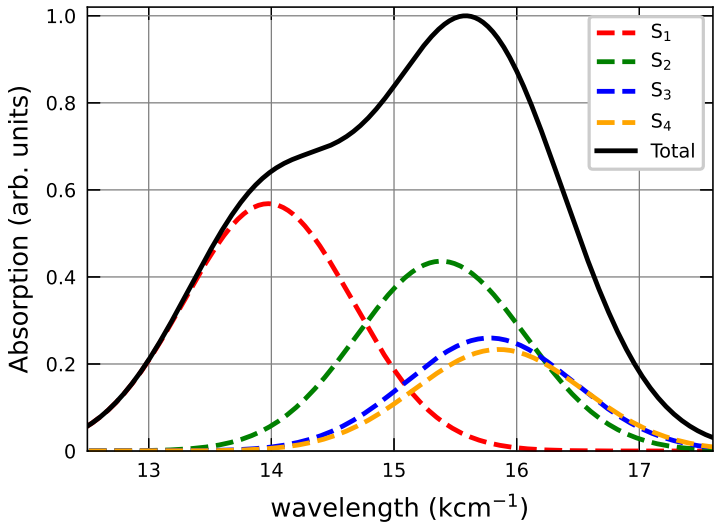

FIG. S8. Simulated absorption spectra of the system using the excited state information from TDDFPT calculations of the last 10000 frames of NVE trajectory.

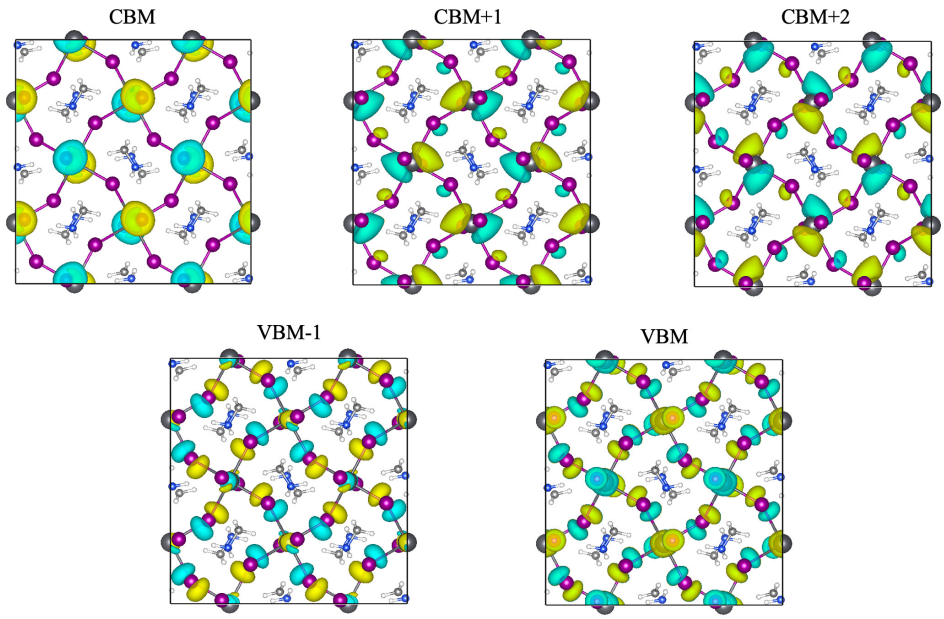

FIG. S9. Real-space distribution of the wave functions for VBM-1, VBM, CBM, CBM+1, and CBM+2. The optimized structure is used for the calculation.

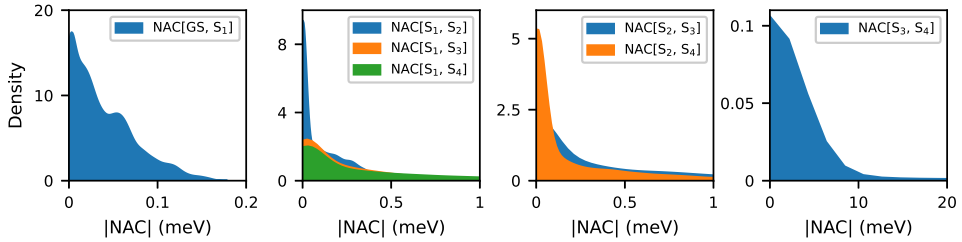

FIG. S10. Distribution of the absolute values of NACs between the states considered in current study.

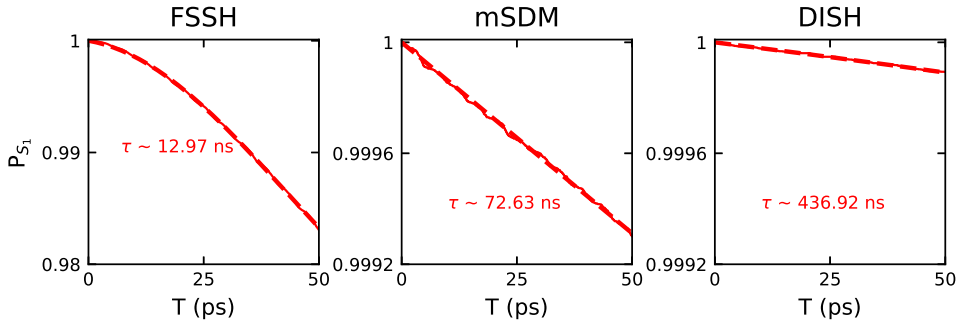

FIG. S11. Electron-hole recombination dynamics from different decoherence correction methods.

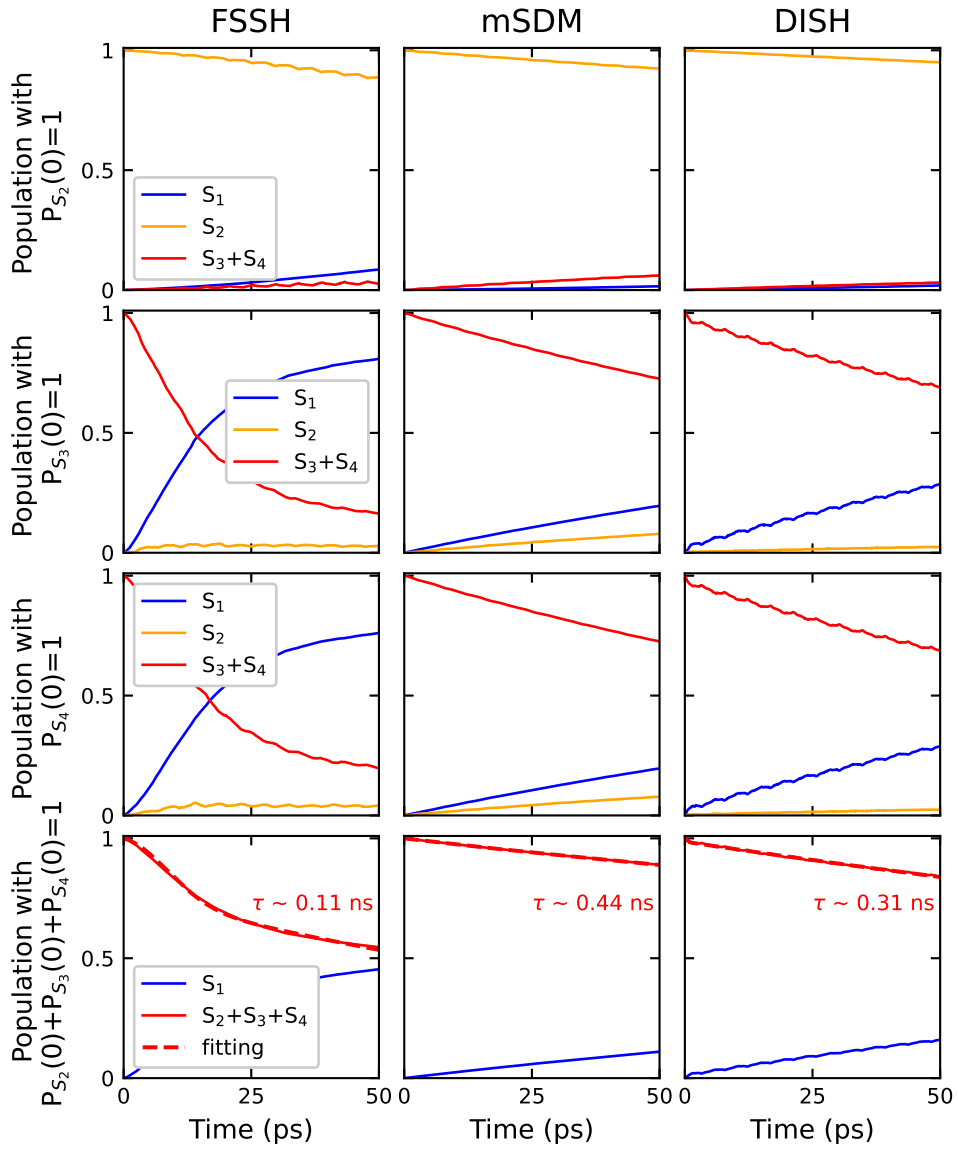

FIG. S12. Population dynamics from different decoherence correction methods with initial population localized on S_2 (row 1), S_3 (row 2), and S_4 (row 3). The lowest row presents the population dynamics on the lowest energy band (S_1, blue) and the second energy band (covering S_2, S_3, and S_4, red).